Soft Matter

PAPER

View Article Online
View Journal | View Issue

Cite this: *Soft Matter*, 2023, **19**, 6691

Light-activated microtubule-based two-dimensional active nematic†

Zahra Zarei,[a] John Berezney,[a] Alexander Hensley,[a] Linnea Lemma,[abc] Nesrin Senbil,[a] Zvonimir Dogic[cd] and Seth Fraden*[a]

Received 2nd March 2023,
Accepted 10th August 2023

DOI: 10.1039/d3sm00270e

rsc.li/soft-matter-journal

We assess the ability of two light responsive kinesin motor clusters to drive dynamics of microtubule-based active nematics: opto-K401, a processive motor, and opto-K365, a non-processive motor. Measurements reveal an order of magnitude improvement in the contrast of nematic flow speeds between maximally- and minimally-illuminated states for opto-K365 motors when compared to opto-K401 construct. For opto-K365 nematics, we characterize both the steady-state flow and defect density as a function of applied light. We also examine the transient behavior as the system switches between steady-states upon changes in light intensities. Although nematic flows reach a steady state within tens of seconds, the defect density exhibits transient behavior for up to 10 minutes, showing a separation between small-scale active flows and system-scale structural states. Our work establishes an experimental platform that can exploit spatiotemporally-heterogeneous patterns of activity to generate targeted dynamical states.

1 Introduction

Active nematics are liquid crystalline materials that use an internal energy source to power autonomous flows.[1] As a paradigmatic example of an internally driven non-equilibrium system, they are intriguing from a fundamental perspective. They also have a potential for diverse applications ranging from microfluidics to autonomous soft robotics. Unbounded active nematics are intrinsically unstable, generating chaotic dynamics.[2–6] Boundaries can transform such chaotic dynamics into ordered flows,[7–16] although it should be noted that no amount of confinement has fully suppressed the creation of topological defects. While boundaries can structure active flows, their fixed nature prevents switching between distinct dynamical states. One route towards this goal is to use external optical signals to control spatiotemporal activity. Recent work has demonstrated optical control of 3D contractile and extensile microtubule (MT)-based isotropic active fluids as well as 2D actin-based active nematics.[17–19]

Light-responsive active matter opens new opportunities for taming the chaotic dynamics of active nematics. For example, optimal control theory predicts the spatiotemporal activity patterns to switch circularly confined nematics from one stable state to another.[20] Complementary theoretical work has focused on optimal designs for moving active nematic droplets through space and creating specific patterns of defects within a material.[21–23] More ambitious control goals are desirable. For instance, one could use feedback to stabilize the active nematic bend instability as it transitions from an aligned to a turbulent state or to reverse the turbulent state into an ordered one.

The first step towards such goals is to design active nematics whose internal dynamics are responsive to external optical signals. Building on previous results, we developed MT-based active 2D nematics and characterized the light-sensitive responses. We focused on two properties: (1) the active nematic flow speeds and (2) the density of topological defects. In each case, we characterized the light-dependent steady-state dynamics as well as transient dynamics as the system switched between two states.

2 Light-sensitive MT-based active materials

2.1 Light-sensitive motor clusters

MT-based active nematics consist of orientationally-aligned micron-long filaments that lack large-scale polar order.[3] The activity is generated by clusters of kinesin motors which simultaneously bind multiple filaments and power relative sliding between anti-parallel MTs. Only linked motor clusters induce interfilament sliding, which generates mesoscopic extensile flows along the nematic axis and thinning flows perpendicular

[a] *The Martin Fisher School of Physics, Brandeis University, Waltham, Massachusetts 02454, USA. E-mail: fraden@brandeis.edu*
[b] *The Department of Chemical and Biological Engineering, Princeton, NJ 08544, USA*
[c] *Department of Physics, University of California, Santa Barbara, California 93106, USA*
[d] *Biomolecular Science and Engineering, University of California, Santa Barbara, California 93106, USA*

† Electronic supplementary information (ESI) available. See DOI: https://doi.org/10.1039/d3sm00270e

to the axis.[24] Conventional clusters consist of truncated biotin-labeled kinesin-1 molecular motors that are permanently bound with streptavidin.[3,25,26] Recently, light-sensitive motor clusters have been introduced.

This work used two previously developed light-sensitive kinesin constructs to power active nematics. The first, opto-K401, is based on the N-terminal 401 amino acid fragment of Drosophila kinesin-1 motor (K401).[27] Two K401 proteins associate to form a two-headed homo-dimeric processive kinesin motor. K401 remains continuously bound to a single MT while taking about one hundred 8 nm "hand-over-hand" steps toward the MT plus-end before detaching.[28] The second type of motor cluster is formed from the 365 N-terminal amino acids of the Drosophila kinesin-1 motor (K365).[26,29] Lacking the dimerization domain, the K365 motor proteins remain monomeric, detaching from MTs after each step.[27,30,31]

Kinesin clusters whose formation is light-dependent were previously used to power both contractile and extensile 3D isotropic MT fluids (Fig. 1).[19,32] These kinesin motors were imbued with light sensitivity through fusion with optically-responsive hetero-dimerizing domains, "iLID" (improved light-induced dimers) and "micro". In the absence of blue light, the binding affinity of iLID to its binding partner, micro, is low.[33] In the presence of blue light, iLID, and micro bind to each other with a 50-fold increase in affinity. To create a light-sensitive motor cluster, several kinesin chimeras were formed. Kinesin fragments K401 and K365 were fused with both iLID (kinesin-iLID) or micro (kinesin-micro). Kinesin clusters formed when these species bind to each other, a process that is enhanced by blue light (Fig. 1).

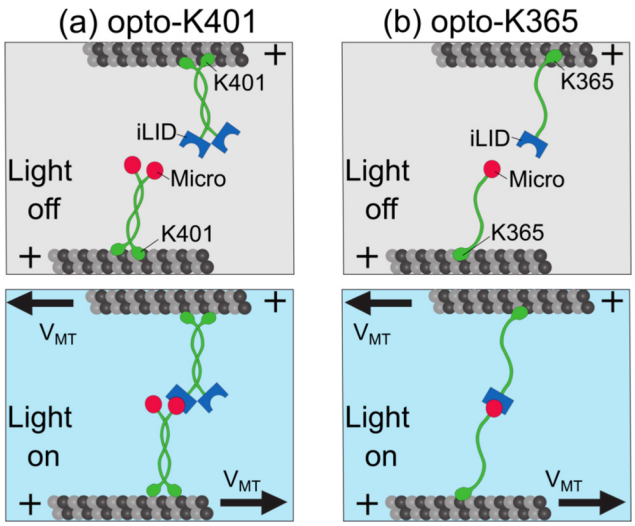

Fig. 1 Light-sensitive protein domains, iLID and micro, are fused to truncated kinesin motors, K401 and K365. They form motor clusters under applied light which generate MT sliding. (a, top) In the absence of blue light, iLID and micro domains have low binding affinity and do not form motor clusters. The homodimeric K401 domains are individually processive and walk along the MTs, but cannot generate interfilament sliding. (a, bottom) Illuminated opto-K401 motor clusters form heterodimeric iLID-micro linkages. These crosslinks transmit stress between MTs, causing their relative movement. (b, top) Individually, the K365 motor domains do not dimerize and are non-processive. Un-illuminated opto-K365 motors do not form motor clusters and, therefore, no sliding is observed. (b, bottom) Upon illumination, the iLID and micro domains form crosslinks, allowing the motor domains to generate interfilament sliding.

3 Materials and methods

3.1 Assembling active nematics

Opto-K401 and opto-K365 were purified as described elsewhere.[17,19] The other components of the active mixture were similar to those used for preparations of conventional 2D MT-based active nematics.[34] Stabilized MTs were prepared by copolymerizing a mixture of tubulin and AlexaFluor-647 dye-labeled tubulin, in the presence of guanosine-5′-[(α,β)-methyleno]triphosphate (GMPCPP). The opto-kinesin pairs (kinesin-iLID and kinesin-micro) were combined with the MTs to achieve a final concentration of 0.03 mg mL^{-1} for each motor. Non-motor reagents were included at concentrations described previously 1.3 mg mL^{-1} tubulin, 0.64% [w/v] polyethylene glycol (35 kDa), 5.5 mM dithiothreitol, 1.42 mM adenosine triphosphate, 3.3 mg mL^{-1} glucose, 22 mg mL^{-1} glucose oxidase, 0.039 mg mL^{-1} catalase, 3.28 mM magnesium chloride, 26.7 mM phosphoenolpyruvate, and 2.8% [v/v] pyruvate kinase/lactate dehydrogenase solution (Sigma P0294-5ML).[34]

A 2D MT-based nematic was formed at an oil/water interface, which was produced by modifying the surfaces of the flow chamber; the lower glass surface was treated with the perfluorinated product, Aquapel, while the upper glass was covered with hydrophilic polyacrylamide brush.[35] Surface-modified channels were filled with a perfluorinated oil (HFE-7500, RAN Biotechnologies) saturated with a fluorosurfactant at 5% w/v (008-FluoroSurfactant, RAN Biotechnologies). An aqueous solution of the 2D nematic components was introduced with a pipette through one side of the chamber. Simultaneously, the oil was removed from the opposite side with a tissue. The different chemistries of the upper and lower glass surfaces led to a separation of the water and oil along the chamber height (z direction), establishing an interface in the image (x–y) plane. The bottom surface was covered with a thin layer of perfluorinated oil while the upper volume of the chamber was filled with the aqueous solution containing all proteins (Fig. S5c, ESI†). The cell was sealed with Norland 81 optical adhesive.

The chamber was exposed to saturating intensities (>20 mW cm^{-2}) of continuous blue light which caused the formation of a 3D isotropic active fluid. Over a period of 30 minutes, MTs adsorbed on the oil–water interface, forming a dense 2D active nematic (Fig. S5c, ESI†). Once the 2D nematic was established, patterns of blue activation light were applied to the sample using the computer-controlled projected light pattern. Simultaneously, the sample was imaged with fluorescence microscopy to capture both the structural and dynamical response of 2D active nematics.

3.2 Calibrated spatial patterning of light

We used a Digital Light Processor (DLP, EKB Technologies Ltd, EKB4500MKII P2) to project spatiotemporal patterns of 460 nm light onto the sample. The DLP has a lens that casts a 20.4 mm by 12.7 mm image at a 25 mm working distance. By removing a

stop in the telescopic lens and shortening the working distance by a few millimeters, we generated a focused image of 35 mm x 23 mm. The DLP contains a Digital Micromirror Device consisting of millions of mirrors that can be positioned towards or away from the optical path. Spatial patterns of light with programmable intensity were achieved by adjusting the duty cycle of each of the mirrors between these positions. The overall range of light intensity was adjusted by altering the current to the LED illuminating the mirror array. Patterns were sent to the DLP through MATLAB.

The projector suffers from a decay in brightness away from the image center (Fig. S3 and S4, ESI†). To quantify such vignetting, we placed a bare CCD camera sensor in the microscope sample plane and recorded the intensity across the projected field (Fig. S1 and S2, ESI†). These measurements provided a lookup table mapping the projected intensities to the measured intensities in the sample plane. Using this lookup table, we modified the projected images to compensate for the vignetting.

3.3 Lightpath configurations

Two configurations were used to acquire fluorescence images and apply activation light to the experimental chambers (Fig. S5, ESI†). In the first design, the epi-illumination branch of a Nikon microscope was used for both the projecting patterns of blue activation light and the fluorescence illumination/detection used for imaging (Fig. S5a, ESI†). In the second mode, the path for the projected activation light was separated from the path for fluorescence imaging (Fig. S5b, ESI†). In this case, the projector was mounted onto the sample stage and light patterns were projected onto the sample from above. Such a design allows for the facile acquisition of large-scale tiled scans without interrupting the light activation protocols. A separate optical arm in the reflection geometry was used to illuminate an image using fluorescence microscopy. More details of both designs are provided in the DLP calibration section of ESI.†

The first light path configuration was primarily utilized to analyze the response of the velocity field to activation light. These chambers had dimensions of 3 mm length and 3 mm width, with a height of approximately 100 μm. The second light path configuration was primarily used to analyze the defect densities in the nematic field, whose measurement requires imaging with high resolution over large sample distances to generate statistically significant measurements. In this configuration, up to six independent channels were employed with widths from 3 mm to 6 mm, lengths of 18 mm, and heights of 100 μm.

3.4 Data analysis

The 2D active nematics were imaged using fluorescence microscopy. Analysis algorithms extracted the 2D nematic orientation field from acquired images (Fig. 2(c) and (d)).[36] The location of the topological defects was identified by either custom-written algorithms or by hand counting.[36] Velocity fields describing the nematic flow were measured with particle image velocimetry (PIV) algorithms applied to the fluorescence micrographs (Fig. 2).[37,38] While the PIV interrogation window size was kept constant across all data sets, other parameters were optimized for individual data sets.

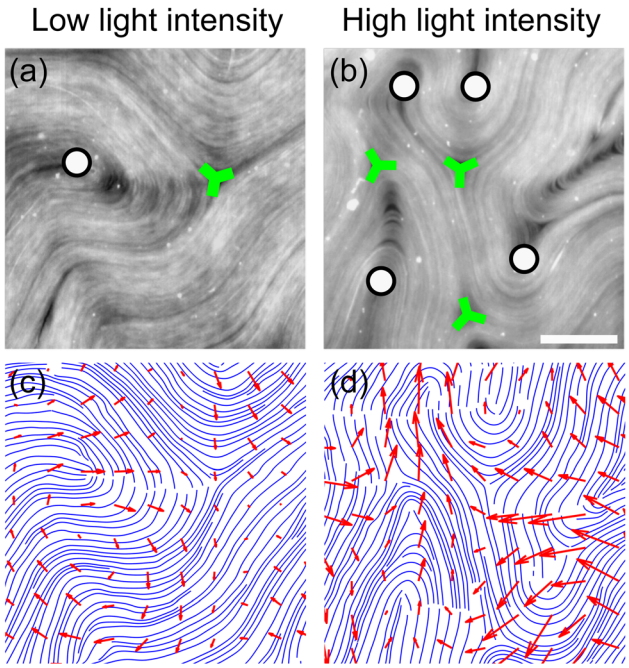

Fig. 2 Light intensity controls the structure and dynamics of light-activated nematics. (a) and (b) Active nematics at low and high intensities exhibit different defect densities. Overlaid circles and triangular crosses show the positions of +1/2 and −1/2 defects respectively. (c) and (d) The nematic director field represented by blue lines and the flow field is represented by red vectors are extracted from fluorescence images. Scale bar, 100 μm.

4 Experimental results

4.1 Light-controlled 2D active nematics

We first replaced streptavidin-based kinesin clusters with opto-K401 motor clusters (*i.e.* homodimerized pairs of both K401-iLID and K401-micro). The concentration of motor clusters was titered until saturating activation light produced dynamics similar to the nematics powered by streptavidin motor clusters. Upon light activation, we observed the formation of a 2D nematic layer at the oil–water interface. Such nematics exhibited topological defects of charge $+\frac{1}{2}$ and $-\frac{1}{2}$. The defect-defect spacing of ∼150 μm was comparable to active nematics powered by conventional motor clusters. When exposed to blue light, active nematics exhibited autonomous motion (Video S1, ESI†). When the light was removed, the defect dynamics decreased but did not halt. To quantify this behavior, we illuminated the left half of an active nematic with light sufficient to generate maximal speed while leaving the right half in the dark. The flows in the illuminated region were 3 μm s^{-1} while the "dark speed" was ∼0.5 μm s^{-1}. The ratio of speeds between the light and dark regions was ∼6 (Fig. S6, ESI†).

4.2 Improving the responsiveness of 2D active nematics

While opto-K401 active nematics exhibited structure and dynamics similar to conventional samples under saturating

light conditions, the light-controlled dynamic range was limited. Ideally, in the dark state, the motor clusters would not crosslink MTs and no active flows would be observed. However, the significant "dark speed" limited the range of achievable light-activated flows. To improve the responsiveness of our system, we evaluated 2D active nematics driven by opto-K365. The constituent proteins of opto-K365, K365-iLID and K365-micro, do not homodimerize due to truncated tail domains (Fig. 1(b)). When illuminated, opto-K365 also generated structure and dynamics resembling conventional 2D active nematics (Fig. 2).

We measured the speed of the nematic as a function of light intensity. Before each measurement at a given intensity, we performed a two-step preparation protocol: "anneal" and "rest". The anneal step consisted of illuminating the sample with a saturating intensity of 20 mW cm^{-2} for 4 minutes. This step produced rapid motion, creating and annihilating of defects as the material approached a steady-state. The rest step consisted of placing the system in the dark for 3 minutes. This ensured that the active dynamics ceased. This procedure generated statistically identical initial conditions before each measurement of the intensity-dependent speed (Fig. 3(a) and (b)).

Using the above-described protocol, we captured how active nematic dynamics depends on the intensity of applied light with fluorescence imaging (Video S3, ESI†). The subsequently extracted PIV-derived velocity fields revealed how light affected the material flows (Fig. 3(a) and (b)). Increasing the illumination intensity leads to an initial nearly linear rise in the steady-state flow speeds, which then saturate at more intense illumination (Fig. 3(e)). The saturation speed varied from day to day, ranging from 1 to 3 μm s^{-1}. A duplicate experiment is presented in Fig. S7 and S8 (ESI†).

We assessed changes in the speed over time (Fig. 3(c)). The maximum speed was ~2 μm s^{-1} and slightly increased over time. For about an hour, the minimum speed was nearly constant at ~25 nm s^{-1}, increasing thereafter. Consequently, the maximum to minimum speed ratio was ~65 for the first hour and then decreased until the active dynamics abruptly ceased after ~2 hours (Fig. 3(d)). This decrease was driven by an increase in the minimum speed.

Biologically-derived materials require special attention, as they can suffer from aging effects such as oxidation and protein aggregation. Aging influenced light-controlled MT-based active nematics after ~1 hour. The dark flow speeds remained constant for about 60 minutes, increasing afterward from a minimum value of 25 nm s^{-1} to 100 nm s^{-1} at 100 minutes, at which time the active dynamics halted (Fig. 3(c)). Likewise, the maximum speed gradually increased in time, by ~20 percent. Thus, the sample showed aging effects after about 60 minutes.

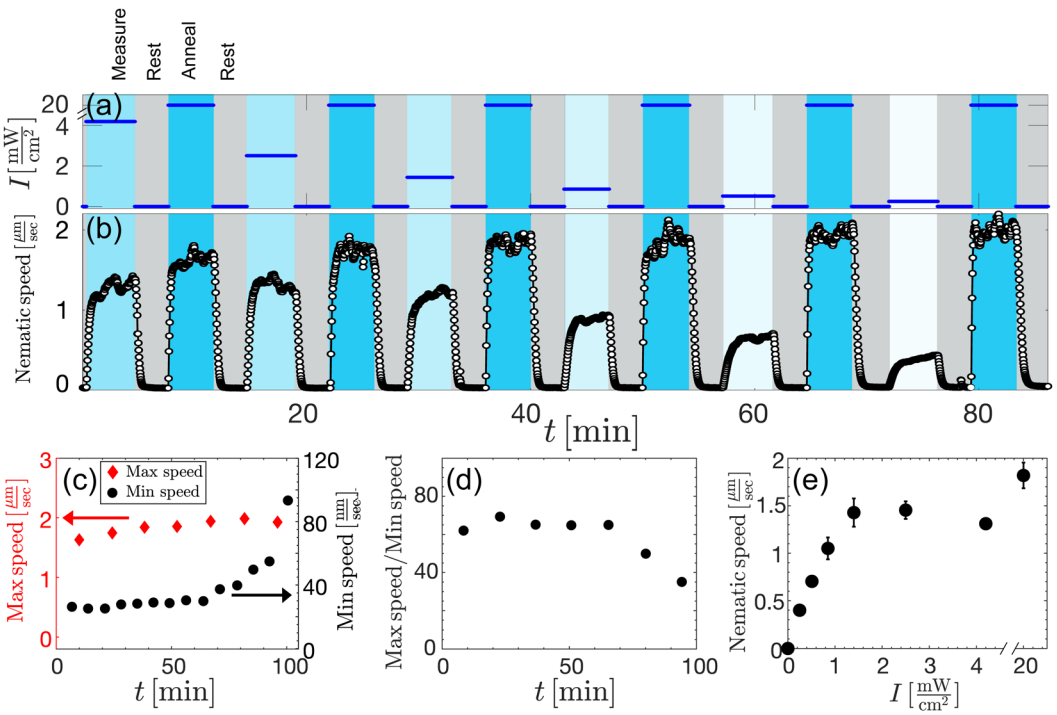

Fig. 3 Light intensity controls the flow speed of opto-K365 active nematics. (a) The time dependence of spatially uniform activation light. The protocol (blue solid line) for applied light intensity, I, contains 4 repeating steps: anneal at 20 mW cm^{-2} for 4 minutes, rest at 0 mW cm^{-2} for 3 minutes, measure at varied intensities for 4 minutes, and rest at 0 mW cm^{-2} for 3 minutes (Video S3, ESI†). (b) The average nematic speed (white circles) plotted against time for time-varying light intensities. The average nematic speed was computed from the spatial average of the PIV flow field in the center of the sample cell (Fig. S5a, ESI†). (c) The maximum nematic speed (red diamonds, left y-axis) observed at saturating light intensity (20 mW cm^{-2}) and the minimum speed (black circles, right y-axis) observed at 0 mW cm^{-2} are plotted as a function of time. Values are steady-state averages extracted from the rest and anneal steps of the light protocol. (d) The ratio of the maximum to minimum speeds as a function of time. (e) The steady-state speed of the active nematic as a function of applied light intensity.

4.2.1 Characterizing transient flow response. We established that the steady-state flow speed is determined by the magnitude of the applied light. External real-time control of active nematics requires an understanding of the transient dynamics in response to light-induced changes. Such transient flow response was quantified by measuring the normalized speed, $|v_n(t)| = |v(t)|/|v_s(t)|$, where $|v(t)|$ is the instantaneous speed and $|v_s(t)|$ is the average steady-state speed.

Following an increase in intensity from 0 to I, the resultant flow speed increased until saturating (Fig. 4(a)). At lower intensities, the nematic reached steady-state speed more slowly. We fitted this data to an exponential function, $|v_n(t)|^{start} = 1 - \exp(-t/\tau_{start})$, and plotted the time constant, τ_{start}, as a function of I. The extracted response time increased with I from ~10 s to 45 s across the full range of applied intensities.

After removing high-intensity illumination, the nematic speed initially remained constant (Fig. 4(b)). However, after a short delay time, t_0, we observed a sharp decrease in speed which saturated at long times as the sample attained its "dark speed". The normalized speed was fitted to an exponential, $|v_n(t)|^{stop} = (1 + \exp((t - t_0)/\tau_{stop}))^{-1}$, where τ_{stop} is the time constant for the speed to decrease to zero and t_0 is the time delay between extinguishing the illumination and when the speed begins to decrease. τ_{stop} is independent of light intensity (Fig. 4(c)) while t_0 grows with increasing applied light intensity (Fig. 4(d)). Data acquired on a different day is in Fig. S9 (ESI†).

4.3 Controlling defect density with light

So far, we quantified how light intensity affects the speed of active nematics. Next, we study how light intensity controls topological defects. We constructed large (18 mm by 5.5 mm) chambers (Fig. 5(a) and Fig. S5b, ESI†). The sample was divided into three spatially-separated illumination zones large enough to collect statistically significant measures of the defect densities while avoiding boundary effects (Fig. S10 and S11, ESI†). Each zone was illuminated with a uniform, but different, light intensity. Changes in the nematic structure were recorded through tiled fluorescence imaging across the chamber (Fig. 5(a)).

This applied light pattern consisted of a central high-intensity region, zone (ii), where the applied light intensity was 2.1 mW cm^{-2}, flanked by two regions of low intensity, zone (i) and zone (iii), illuminated with 0.13 mW cm^{-2}. The defect densities were consistently higher in the high-intensity zones compared to the low-intensity zones (Fig. 5(b)).

The pattern of the activation light was then changed (Fig. 5(c)). Across all the measurements, the defect density increased with increasing intensity. Additionally, regions with equal applied light generated structures with equal defect densities within experimental error, even when separated in time or space. Table 1 lists the measured defect densities in steady-state as a function of applied light. The density increases by 40% between the low and high light intensities. Results from repeated experiments are presented in ESI,† Table S1.

We note that the chamber walls introduced another mechanism which affects defect density separately from light activation. To capture this, we quantified the defect density as a function of distance from the chamber wall. We found the defect density increased by a factor of up to 4 near the wall and deviations from bulk defect density extended hundreds of microns into the chamber (Fig. S10 and S11, ESI†). To separate chamber confinement effects from light-induced effects, all measurements examining light-induced structural changes were taken in the center of the chamber, where the defect density gradient was at a minimum.

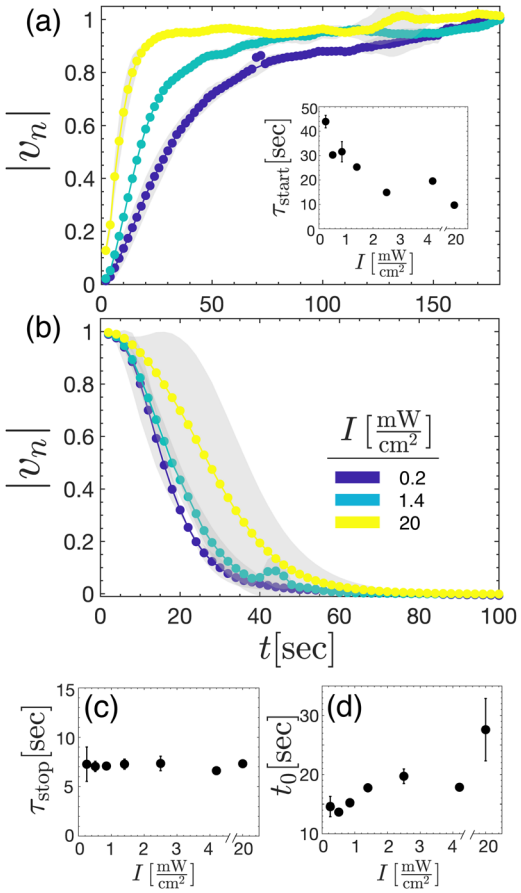

Fig. 4 Transient dynamics in response to changing light intensity. (a) The light intensity is increased from 0 mW cm^{-2} to I. The normalized average nematic flow speed, $\langle|v_n(t)|\rangle$, is the average instantaneous speed, $\langle|v(t)|\rangle$, normalized by the steady-state speed, $\langle|v_s(t)|\rangle$, and increases as a function of elapsed time, t. The grey bands are the standard deviation within the nematic flow field at a given time point. Inset: The characteristic time constant, τ_{start}, extracted from the function, $\langle|v_n(t)|\rangle = 1 - \exp(-t/\tau_{start})$, is plotted against light intensity, I. (b) The applied light intensity is decreased from I to 0 mW cm^{-2}. The normalized speed, $\langle|v_n|\rangle$, is plotted against elapsed time, t. (c) The data in (b) is fit to $(1 + \exp((t - t_0)/\tau_{stop}))^{-1}$. Here, τ_{stop} is plotted against light intensity. (d) The time lag, t_0, is plotted against the applied light intensity.

4.3.1 Transient defect density. Next, we focused on changes in defect density between two steady-states. When the light intensity was increased, the defect density increased monotonically before reaching a steady-state value (Fig. 6(c)). Analogously, with decreasing light intensity, the defect density decreased monotonically before reaching a steady-state (Fig. 6(a) and (b)).

We either increased intensity from low to high ($I_1 \rightarrow I_2$) or reversed ($I_2 \rightarrow I_1$). The time to steady-state was about 4 minutes

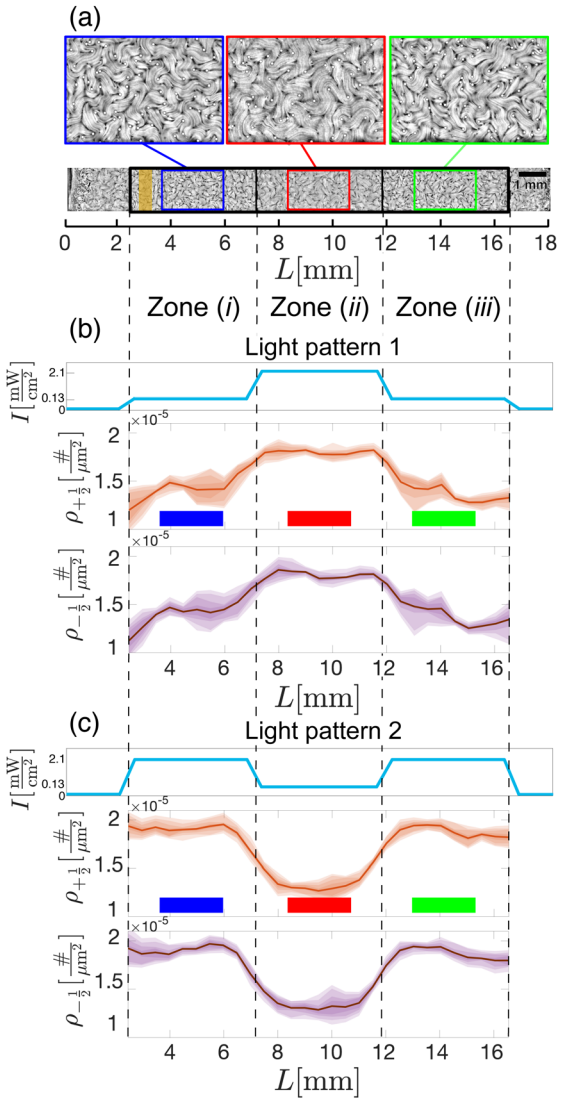

Fig. 5 Spatially-patterned light controls local defect density. (a) A composite of fluorescence micrographs shows an 18 mm × 1.7 mm strip across an active nematic sample (Fig. S5b, ESI†). Three outcropped images outlined in blue, red and green indicate regions where the defect densities were constant and highlight the structural variation between regions of different light illumination. White circles indicate $+\frac{1}{2}$ defects. (b) Vertical dotted lines define zones within the sample onto which uniform intensity blue light is projected. Changes in applied light are blurred over 0.5 mm due to projector defocusing. A schematic representation of the applied light intensity is shown as a function of chamber position (solid cyan line). The moving average defect density is plotted as a function of position (orange and purple lines), including the percentile error as a shaded region. Defect densities are measured for a 15 minute interval after a steady state is achieved. (c) The steady-state population of defects changes when the activation light is changed. A schematic represents the applied light intensity across the sample (solid cyan line). The measured local positive and negative defect densities (solid orange and purple lines) are plotted as a function of position in the sample.

when intensity was increased, while it was about 10 minutes when intensity decreased (Fig. 6(b) and (c)). These timescales are significantly slower than those for nematic flows, which reach steady-state in less than one minute (Fig. 4). The faster response of flow speed may play a role in determining how the rates of defect nucleation and defect creation are imbalanced in these transient periods.

Table 1 Speed and defect density as a function of intensity

Intensity (mW cm^{-2})	Speed (μm s^{-1})	Defect density (#/μm^2)
2.1 (High)	3.05 ± 0.34	(1.91 ± 0.1) × 10^{-5}
0.13 (Low)	1.45 ± 0.17	(1.36 ± 0.1) × 10^{-5}
	$\sqrt{\text{Ratio(High/Low)}}$: 1.44	Ratio (High/Low): 1.4

At intensities greater than ∼2.1 mW cm^{-2}, the nematic speed saturated (Fig. 3(e)). The defect density remained constant as the intensity was changed from 30 mW cm^{-2} to 2.1 mW cm^{-2} (Fig. 6(d)). If the flow speed serves as a proxy for activity, then one expects the defect density to change only when the speed also changes.

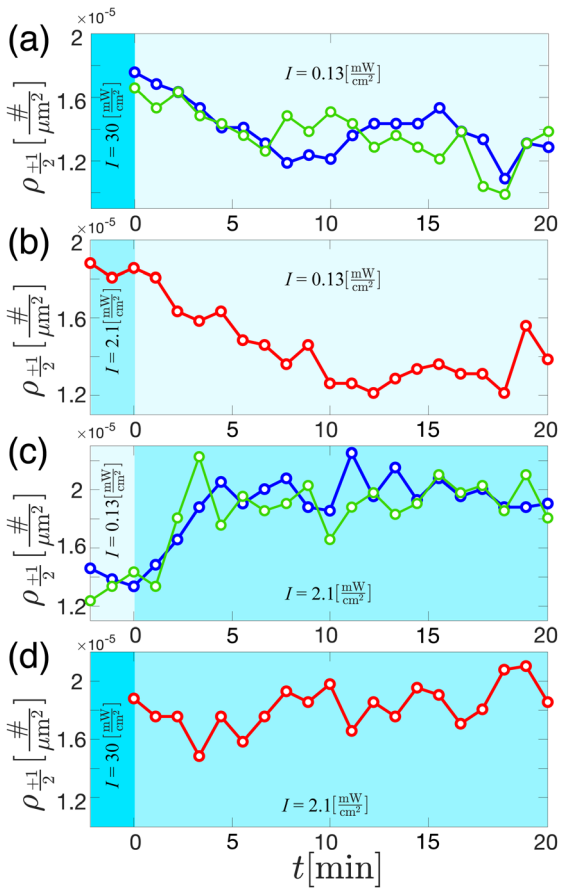

Fig. 6 Transitions to steady-state $+\frac{1}{2}$ defect density after changes in activation light. Measured defect density is plotted after changes in applied light intensity (blue, red and green circles). Plotted colors (blue, red, and green) indicate the outcropped area defined in Fig. 5(a) (a) Defect density ($\rho_{+\frac{1}{2}}$) is plotted against time (t) as intensity is changed from 30 mW cm^{-2} to 0.13 mW cm^{-2} at t = 0. (b) Defect density is plotted against time as intensity decreased from 2.1 mW cm^{-2} to 0.13 mW cm^{-2}. (c) Defect density is plotted against time when intensity is increased 0.13 mW cm^{-2} to 2.1 mW cm^{-2}. (d) Defect density remains steady over time when intensity changes from 30 mW cm^{-2} to 2.1 mW cm^{-2}.

4.3.2 Scaling of defect density with nematic speed. The structure and density of defects within active nematics have been extensively studied. Defect density is dependent on activity, α, which is, in turn, proportional to the nematic speed: $|v| \propto \alpha$.[39] Theoretical models and experimental results find different scaling behavior of defect density with activity α, ranging from $\rho \propto \sqrt{\alpha}$ to $\rho \propto \alpha$.[39–41]

We found the steady-state defect density, $\rho(I)$, increases with increasing steady-state speed, $|v(I)|$ (Fig. 7). We have applied one-parameter fits, fixing the value of ρ to zero at $|v| = 0$. The $\rho \propto \sqrt{\alpha}$ fit outperforms the linear fit, giving R^2 values of 0.86 and 0.47, respectively. As a word of caution, we note that data for defect density varies only by a factor of 1.4 (Table 1 and Table S1, ESI†).

5 Discussion & outlook

We quantified the ability of light-activated kinesin motor clusters to drive non-equilibrium dynamics of 2D active nematics. We characterized the steady-state and transient response of the nematic flow to changes in the activation light intensity. By utilizing Opto-K365 in place of Opto-K401, we optimized the system to have light-responsive flow speeds ranging from 0.025 μm s^{-1} to 2 μm s^{-1}. We also characterized the steady-state and transient response of the defect density to changes in light intensity. Similar to previous work,[19] we found that non-processive opto-K365 reduced the dark flow of active MT materials. Interestingly, this improvement was more pronounced in 2D active nematics than in isotropic 3D active fluids. These results lay the groundwork to use spatiotemporal patterns of light to prescribe the active dynamics of 2D nematic materials.

Our results show the on-rate of nematic flow is dependent on the intensity of light. We assume this is a consequence of the opotogenetic domain binding of the kinesin motors and their subsequent driving of the microtubule flow. In contrast, the off-rate of nematic flow is independent of the intensity of light. We assume this is a consequence of light-independent motor cluster unbinding. However, it remains a challenge to connect the binding of motor clusters and how these microscopic constituents organize at the molecular level to produce the nematic flow which we observe and characterize.[42–44] A better understanding of these mechanisms would help the rational design of improved experimental systems.

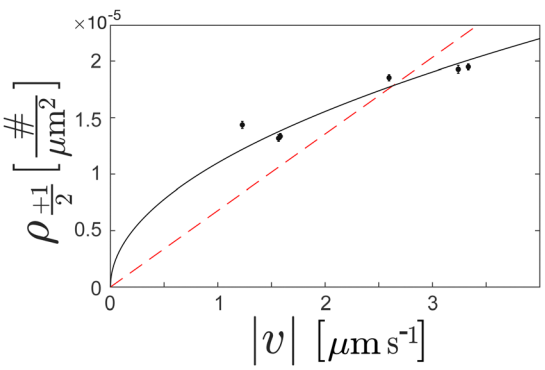

Fig. 7 Defect density ($\rho_{\pm\frac{1}{2}}$) increases with the speed (v) of an active nematic (black circles). Fits are to $\rho \propto |v|^{1/2}$ (black solid line) and $\rho \propto |v|$ (red dashed line).

The cessation of active nematic flow speed exhibited an unexpected lag time, t_0, before the speed started to decrease (Fig. 4 and Fig. S9d, ESI†). This lag time increased with intensity, saturating at high values. To explain this observation we make several assumptions (Fig. S12, ESI†): (1) it takes time for the optogenetic binding partners to dissociate after the removal of light, (2) the concentration of bound clusters increases with increasing intensity, $c_b(I)$, (3) above a critical concentration of bound domains the nematic speed saturates (c_v), and (4) it is possible for $c_b(I)$ to be below or above c_v. These assumptions predict that delay time $t_0 = 0$ when the intensity is low enough that the speed is not saturated, $c_b(I) < c_v$. In this limit, the speed reduces when clusters unbind. However, when $c_b(I) > c_v$, the concentration of clusters must decrease below c_v for the speed to decrease. This process takes time, so t_0 increases with intensity once the speed has saturated.

In a steady state, we observed that the applied light more strongly affects flow speed than defect density. Further, the defect density dependence on the flow speed appears to follow the relation, $\rho \propto \sqrt{v}$. Outside of steady-state behavior, flows respond to changes in light intensity faster in comparison to changes in defect density. A new steady state must evolve through transient processes that involve defect creation and annihilation. Our results show that active nematics attain steady state speeds before defect-related structural changes take place. It will be interesting to theoretically examine the transient pathways by which these changes occur and how specific spatiotemporal patterns of light can modify and perturb these processes.

The rate at which defect density increases with increasing illumination is faster than the rate at which defect density decreases to a lower steady-state (Fig. 6(b) and (c)). In steady-state, the rate of defect annihilation and defect creation is balanced.[39,45] In contrast, during the transient period between steady states, these rates cannot be equal. Annihilation requires two oppositely charged defects to join, which depends on both their density and speed. In contrast, creation does not require collision but increases with activity. These observations suggest that the process of defect creation responds more quickly than annihilation.

Two experimental parameters determined nematic defect density: the distance to the chamber wall and the activation light intensity. These two effects complicated the interpretation of our experiments. Generally, the wall-induced effect on defect density was stronger than those observed from light-induced structural changes (Fig. S10 and S11, ESI†). It is notable that, as one moves from the wall, the density of defects decreases and the velocity increases whereas the inverse is observed in light-induced defects: as light intensity is increased, both the velocity and density increase. This suggests there are two independent mechanisms for generating defects. Near the wall, the defect

density is set by viscous dissipation in the third dimension whereas the defect density is set by activity in the bulk. Previous experimental work has established that dissipation can control defect density in active nematics.[11,46] However, the discrepancy in lengthscales between the oil height and the defect density remains unexplained (Fig. S10 and S11, ESI†).

We characterized the basic parameters needed to carry out spatiotemporal control of 2D microtubule nematics. A significant challenge is to increase the lifetime of opto-active nematics before the onset of aging effects (1 hour) with respect to the annealing time of defects (10 minutes). Active nematic aging was most apparent in the dark state speed, while the maximum speed under high-intensity illumination changed little over time. This might be a consequence of the non-specific aggregation of motor proteins over time. Consequently, creating nematics with substantially increased longevity is the most important experiment hurdle to creating fully controllable 2D active nematics. Diffusion chambers, which constantly restock substrate chemicals such as ATP or motor proteins, may help extend the sample lifetimes.

Author contributions

SF, JB, and ZD conceptualized experiments. JB, LL, and AH provided supervision. SF and JB wrote the paper. ZD edited the paper. NS conducted initial experiments on K401. ZZ conducted the experiments on K365, data analysis, and paper visualization.

Conflicts of interest

There are no conflicts to declare.

Acknowledgements

This work was primarily supported by Brandeis Bioinspired Soft Materials MRSEC-2011846. The development of the instrument for projecting spatial light patterns was supported by the Department of Energy (DOE), Office of Basic Energy Sciences through project DE-SC0022291.

Notes and references

1 M. C. Marchetti, J. F. Joanny, S. Ramaswamy, T. B. Liverpool, J. Prost, M. Rao and R. A. Simha, *Rev. Mod. Phys.*, 2013, **85**, 1143–1189.
2 R. A. Simha and S. Ramaswamy, *Phys. Rev. Lett.*, 2002, **89**, 058101.
3 T. Sanchez, D. T. Chen, S. J. DeCamp, M. Heymann and Z. Dogic, *Nature*, 2012, **491**, 431–434.
4 S. Zhou, A. Sokolov, O. D. Lavrentovich and I. S. Aranson, *Proc. Natl. Acad. Sci. U. S. A.*, 2014, **111**, 1265–1270.
5 N. Kumar, R. Zhang, J. J. de Pablo and M. L. Gardel, *Sci. Adv.*, 2018, **4**, eaat7779.
6 1971.
7 F. C. Keber, E. Loiseau, T. Sanchez, S. J. DeCamp, L. Giomi, M. J. Bowick, M. C. Marchetti, Z. Dogic and A. R. Bausch, *Science*, 2014, **345**, 1135–1139.
8 A. Doostmohammadi, M. F. Adamer, S. P. Thampi and J. M. Yeomans, *Nat. Commun.*, 2016, **7**, 10557.
9 M. M. Norton, A. Baskaran, A. Opathalage, B. Langeslay, S. Fraden, A. Baskaran and M. F. Hagan, *Phys. Rev. E*, 2018, **97**, 012702.
10 A. Opathalage, M. Norton, M. Juniper, B. Langeslay, S. Aghvami, S. Fraden and Z. Dogic, *Proc. Natl. Acad. Sci. U. S. A.*, 2019, **116**, 4788–4797.
11 K. Thijssen, D. A. Khaladj, S. A. Aghvami, M. A. Gharbi, S. Fraden, J. M. Yeomans, L. S. Hirst and T. N. Shendruk, *Proc. Natl. Acad. Sci. U. S. A.*, 2021, **118**, e2106038118.
12 L. Zhao, L. Yao, D. Golovaty, J. Ignés-Mullol, F. Sagués and M. Carme Calderer, *Chaos*, 2020, **30**, 113105.
13 J. Hardoüin, R. Hughes, A. Doostmohammadi, J. Laurent, T. Lopez-Leon, J. Yeomans, J. Ignés-Mullol and F. Sagués, *Commun. Phys.*, 2019, **2**, 121.
14 P. Chandrakar, M. Varghese, S. A. Aghvami, A. Baskaran, Z. Dogic and G. Duclos, *Phys. Rev. Lett.*, 2020, **125**, 257801.
15 D. Rivas, T. Shendruk, R. Henry, D. Reich and R. Leheny, *Soft Matter*, 2020, **16**, 9331–9338.
16 T. Gao, M. D. Betterton, A.-S. Jhang and M. J. Shelley, *Phys. Rev. Fluids*, 2017, **2**, 093302.
17 T. D. Ross, H. J. Lee, Z. Qu, R. A. Banks, R. Phillips and M. Thomson, *Nature*, 2019, **572**, 224–229.
18 R. Zhang, S. A. Redford, P. V. Ruijgrok, N. Kumar, A. Mozaffari, S. Zemsky, A. R. Dinner, V. Vitelli, Z. Bryant and M. L. Gardel, *et al.*, *Nat. Mater.*, 2021, **20**, 875–882.
19 L. M. Lemma, M. Varghese, T. D. Ross, M. Thomson, A. Baskaran and Z. Dogic, *Proc. Natl. Acad. Sci. U. S. A.*, 2023, **2**, pgad130.
20 M. M. Norton, P. Grover, M. F. Hagan and S. Fraden, *Phys. Rev. Lett.*, 2020, **125**, 178005.
21 S. Shankar, V. Raju and L. Mahadevan, *Proc. Natl. Acad. Sci. U. S. A.*, 2022, **119**, e2121985119.
22 S. Shankar, L. V. Scharrer, M. J. Bowick and M. C. Marchetti, *arXiv*, arXiv:2212.00666, 2022, preprint.
23 M. J. Falk, V. Alizadehyazdi, H. Jaeger and A. Murugan, *Phys. Rev. Res.*, 2021, **3**, 033291.
24 L. M. Lemma, M. M. Norton, A. M. Tayar, S. J. DeCamp, S. A. Aghvami, S. Fraden, M. F. Hagan and Z. Dogic, *Phys. Rev. Lett.*, 2021, **127**, 148001.
25 F. J. Nédélec, T. Surrey, A. C. Maggs and S. Leibler, *Nature*, 1997, **389**, 305–308.
26 P. Chandrakar, J. Berezney, B. Lemma, B. Hishamunda, A. Berry, K.-T. Wu, R. Subramanian, J. Chung, D. J. Needleman and J. Gelles, *et al.*, *Soft Matter*, 2022, **18**, 1825–1835.
27 E. Berliner, E. C. Young, K. Anderson, H. K. Mahtani and J. Gelles, *Nature*, 1995, **373**, 718–721.
28 A. Yildiz, M. Tomishige, R. D. Vale and P. R. Selvin, *Science*, 2004, **303**, 676–678.
29 A. M. Tayar, M. F. Hagan and Z. Dogic, *Proc. Natl. Acad. Sci. U. S. A.*, 2021, **118**, e2102873118.

30 J. J. Correia, S. Gilbert, M. Moyer and K. Johnson, *Biochemistry*, 1995, **34**, 4898–4907.
31 W. O. Hancock and J. Howard, *J. Cell Biol.*, 1998, **140**, 1395–1405.
32 T. D. Ross, H. J. Lee, Z. Qu, R. A. Banks, R. Phillips and M. Thomson, *Nature*, 2019, **572**, 224–229.
33 G. Guntas, R. A. Hallett, S. P. Zimmerman, T. Williams, H. Yumerefendi, J. E. Bear and B. Kuhlman, *Proc. Natl. Acad. Sci. U. S. A.*, 2015, **112**, 112–117.
34 A. M. Tayar, L. M. Lemma and Z. Dogic, *Microtubules*, Springer, 2022, pp.151–183.
35 A. W. C. Lau, A. Prasad and Z. Dogic, *EPL*, 2009, **87** 48006.
36 M. M. Norton, qcon-nematicdefectfinder, 2023, **https://github.com/wearefor/qcon_nematicdefectfinder**.
37 W. Thielicke and R. Sonntag, *J. Open Res. Softw.*, 2021, **9**, 1.
38 W. Thielicke, *Diss. University of Groningen*, 2014.
39 S. Thampi, R. Golestanian and J. Yeomans, *Philos. Trans. R. Soc., A*, 2014, **372**, 20130366.
40 E. J. Hemingway, P. Mishra, M. C. Marchetti and S. M. Fielding, *Soft Matter*, 2016, **12**, 7943–7952.
41 L. M. Lemma, S. J. DeCamp, Z. You, L. Giomi and Z. Dogic, *Soft Matter*, 2019, **15**, 3264–3272.
42 T. Gao, R. Blackwell, M. A. Glaser, M. D. Betterton and M. J. Shelley, *Phys. Rev. Lett.*, 2015, **114**, 1–5.
43 G. A. Vliegenthart, A. Ravichandran, M. Ripoll, T. Auth and G. Gompper, *Sci. Adv.*, 2020, **6**, eaaw9975.
44 S. Fürthauer, B. Lemma, P. J. Foster, S. C. Ems-McClung, C.-H. Yu, C. E. Walczak, Z. Dogic, D. J. Needleman and M. J. Shelley, *Nat. Phys.*, 2019, **15**, 1295–1300.
45 L. Giomi, L. Mahadevan, B. Chakraborty and M. F. Hagan, *Nonlinearity*, 2012, **25**, 2245–2269.
46 P. Guillamat, J. Ignés-Mullol, S. Shankar, M. Marchetti and F. Sagués, *Phys. Rev. E*, 2016, **94**, 226–234.